Li, Zhongsen; Blanc, Matthieu; Thorel, Luc

Using FBGS to estimate the horizontal response of a monopile in a geotechnical centrifuge

Published in:
International Journal of Physical Modelling in Geotechnics

DOI:
10.1680/jphmg.19.00022

Published: 01/05/2020

Document Version
Peer-reviewed accepted author manuscript, also known as Final accepted manuscript or Post-print

Please cite the original version:
Li, Z., Blanc, M., & Thorel, L. (2020). Using FBGS to estimate the horizontal response of a monopile in a geotechnical centrifuge. *International Journal of Physical Modelling in Geotechnics*, *20*(3), 164-174. Article 1900022. https://doi.org/10.1680/jphmg.19.00022

Using Fibre Bragg Grating sensors to estimate the horizontal response of a monopile in geotechnical centrifuge

Zhong-Sen Li, post-doctor[1, 2]; Matthieu Blanc, researcher[1*]; Luc Thorel, senior researcher[1]

[1] Laboratory of Geomaterials and Modelling in Geotechnics, Department GERS, IFSTTAR, Route de Bouaye, Bouguenais 44344, France
[2] Department of Civil Engineering, Aalto Univeristy, Otaniemi 02150, Finland

* Corresponding author: matthieu.blanc@ifsttar.fr, +33 2 40 84 58 18

Abstract: A 50-mm-diameter circular aluminium tube was instrumented with two optical fibres that consist of 13 Fibre Bragg Grating sensors (FBGS) for each. The performance of the FBGS was evaluated by applying a series of increasing transversal loads at 1×g level and comparing the strains measured by FBGS with those calculated from the Euler-Bernoulli beam theory. Centrifuge test was then conducted at 100×g to estimate the transversal response of the calibrated model pile that had been jacked 450 mm into saturated sand and horizontally loaded at 500 mm above the ground. The profiles of the normal strain, bending moment, soil reaction and pile deflection were measured or determined, allowing to construct the soil reaction – pile deflection (P-y) curves. The results confirmed the reliability of the FBGS at 100×g by giving satisfactory measurements on bending moments and coherent measurements on shear force at the ground level.

Key words: Centrifuge; Monopile; Transversal loading; Fibre Bragg Grating sensors; Sand

Manuscript revised: ***2019-11-01***
Number of words: ***3746***
Number of Table: ***2***
Number of Figure: ***8***

List of notation

P	soil reaction (kN/m)
y	pile deflection (mm)
ε	normal strain of the pile
λ	peak wavelength of the fibre Bragg grating (nm)
$\Delta\lambda$	peak wavelength shift (nm)
k	gage factor of the optical fibre
E	Young modulus (GPa)
I	moment of inertia of an area (m^4 or mm^4)
F	applied vertical weight during pile calibration (N)
D	external diameter (mm)
d	inner diameter (mm)
M	bending moment (N.m)
L	Embedded pile length (m)
l	lever arm (mm)
L	embedded pile length (m)
H	applied horizontal force at the pile head (N)
V	shear force (N)
g	gravitational acceleration (m/s^2)
$d_{10}/d_{50}/d_{60}$	diameter at which 10, 50 or 60% of the sample's mass is comprised of smaller particles (µm)
$\rho_{d\text{-}min}$	minimum dry density (g/cm^3)
$\rho_{d\text{-}max}$	maximum dry density (g/cm^3)
Λ	distance between two adjacent fringe (nm)
n	positive integer
z	depth of the pile embedment (mm)
C_u	coefficient of uniformit

1. Introduction

Monopile is a typical foundation for offshore wind farms. It takes over 80% of recently installed wind turbines (Wind Europe, 2017) and represent about 15-20% of the total investment. The lifecycle of the monopile is influenced by the horizontal service loads resulting from winds, currents and waves. The generation of horizontal deflection may degrade the foundation soil and as a result trigger the instability problems. Faced with the increasing capacity of the next-generation wind turbines, the dimension of the future monopiles is expected to increase, for example, to as large as 10 m in diameter. For such large-diameter monopiles, current design codes for long and slender piles are deemed inappropriate and new standards need to be developed.

In the literature, three experimental methods exist to characterise the response of pile or monopile under transversal loads: i) the full-scale field tests (e.g. Davisson and Salley, 1969; Baguelin et Jézéquel, 1972, Cox et al., 1974; Reese et al., 1974; Ting, 1987; Little and Briaud, 1988; Koukoura et al., 2015; Barbosa et al., 2017; Jardine et al., 2018; McAdam et al., 2018); ii) reduced-scale laboratory tests (e.g. LeBlanc et al., 2010; Abadie et al., 2018) and iii) reduced-scale centrifuge tests (e.g. Georgiadis et al., 1992; Verdure et al., 2003; Rosquoet et al., 2007; Li et al., 2010; Klinkvort and Hededal, 2013, 2014; Klinkvort et al., 2013, 2019; Choo and Kim, 2015; Truong et al., 2018). Each above-mentioned method presents its own inherent advantages and disadvantages. For performing parametric studies in a first step, reduced-scale laboratory and centrifuge tests are more feasible due to the consideration of testing budget. Comparing to laboratory tests, centrifuge tests at elevated gravity have the advantage of reproducing the field stress condition for monopiles. Through carrying out centrifuge tests, researchers were able to test monopiles as large as 50 mm in diameter (e.g. Li et al, 2010, Klinkvort et al., 2019). The pile local strains were measured and then used to determine the soil reaction – pile deflection (P-y) relationship. These results, together with the full-scale field tests and reduced-scale laboratory tests, are of interest for the design of next generation monopiles.

The present study is part of the SOLCYP+ project (France Energies Marines, 2017), which is an extension of the SOLCYP project (Puech and Garnier, 2017). The main objective was to experimentally investigate the response of the model piles under horizontal load in geotechnical centrifuge and then to extrapolate the prototype pile behaviour. Fibre Bragg Grating sensors (FBGS) were used to measure the local strains and to determine the moment profile of the pile. Experimental results are presented following the local pile analysis (Garnier, 2013).

2. Principle and geotechnical application of FBGS

Exposing the Germanium-doped optical fibre to the spatial pattern of ultraviolet light (e.g. Hill and Meltz, 1997; Kreuzer, 2006) can artificially alter the refractive index of the fibre and form a periodic modulation of the refractive index (i.e., grating). When a beam of light passes a grating, part of the light will be reflected and the other be transmitted. The reflected lights accumulate and form a peak if an integer of the light wavelength fits into two times of the fringe spacing, as shown in Figure 1.

Under the effect of the external stress or temperature, the optical fibre shrinks or swells. This shrinkage-swelling results in a change in grating period and as a result a corresponding shift of the reflected peak wavelength in the recorded spectra. Under temperature-controlled condition, the strain (ε) can be calculated with the peak wavelength shift ($\Delta\lambda$) by the following formula:

$$\varepsilon = \frac{\Delta\lambda}{\lambda k} \tag{1}$$

where λ (nm) is the initial peak wavelength under null external stress (i.e., reference scan), $\Delta\lambda$ (nm) is the peak wavelength shift and k, the gage factor, is equal to 0.78 for the fibre used in this study.

As the FBGS has very small dimension (e.g., diameter of several hundred micro-meters), it can be adhered on or embedded into the piles or beams without significantly changing their geometry and mechanical property. For such reason, it has been increasingly used. In geotechnical laboratory and field testing, FBGS have been used to measure the load transfer of the model pile (e.g., Lee et al., 2004), the strain distribution along the soil nails during pull-out test (e.g., Zhu et al., 2007, 2011; Hong et al., 2017) and the transversal displacement of ballast under cyclic loading conditions (e.g., Hussaini et al., 2015). Besides, FBGS have been used to monitor the dynamic process of the wind turbine blades (e.g., Park et al., 2011), large pile under vertical driving conditions (e.g., Doherty et al., 2015) and strains of buried pipelines under different external loads (e.g. Glisic and Yao, 2012; Simpson et al., 2015; Ni et al., 2018).

However, the report of the FBGS in geotechnical centrifuge is limited. Kapogianni et al. (2010) investigated the performance of FBGS in a drum centrifuge at ETH Zurich. The FBGS gave coherent measurements at different g-level (0-100 g) even though the unstable measuring signal was observed due to the movements of the FBGS cables. Da Silva et al. (2016) reported their experience on FBGS instrumentation and calibration in centrifuge test at the University of Cambridge. A first issue that they considered was the location and orientation of the fibre optic interrogator. In their study, the interrogator was placed on the centrifuge beam as close as possible to the centre to minimise the gravitational acceleration experienced by the interrogator. In addition, the interrogator box was orientated such that the axis of the fans aligned with the direction of the gravitational acceleration to minimise impact of g-level on the operation of the interrogator. After these efforts, the authors found that the interrogator remained securely in place with g-level up to 40 g (i.e., 6 g for the interrogator). Excellent correlation was achieved between the strains measured by FBGS and those by LVDT, with the difference generally smaller than 5%. To avoid the high g-forces within the interrogator, Correia et al. (2016) reported a new method to place the FBGS interrogator. This method consists of using a fibre optic rotary joint and placing the interrogator outside of the centrifuge. At Chang'an University (China), Weng et al. (2016) conducted a series of centrifuge tests, using both FBGS and strain gauge to measure the vertical strains of a jacked steel pile previously soaked by water. The difference between the strains measured by FBGS and the strains measured by strain gauges was, in most cases, within 10%.

In conclusion, the FBGS i) provides a precise, reliable and convenient method to monitor strain change of piles and pipes; ii) allows multiple strain measurements with a single fibre; iii) is easy to be installed and suitable under both static and dynamic load conditions and iv) is rarely used in geotechnical centrifuge. Compared to the strain measuring methods that the authors previously adopted (e.g., gluing the strain gages outside or even inside the tube in Rosquoët et al., 2007 and El Haffar et al., 2019), the choice of the optical fibres in this study was mainly to maintain the wall thickness of the tube while working on an open-ended model pile.

3. Instrumentation and calibration of the model pile

The geometric and mechanical characteristics of the model pile are described in Figure 2 and Table 1. The choice of an aluminium tube instead of a steel bar allows to respect the key scale factor of the rigidity (*EI*) while maintaining a suitable tube thickness for embedding FBG sensors. Besides, aluminium has been commonly used in geotechnical centrifuge to reproduce the behaviour of steel structures (e.g. Ng et al., 2015; Saiyar et al., 2016). The pile was chiselled with two semi-cylindrical grooves that are diametrically opposed. The radius of the grooves is 0.5 mm, i.e., 1/5 the wall thickness of the pile. Two 200-micrometer-diameter optical fibres were laid straight in the grooves and then sealed by a bi component cold curing epoxy, i.e., X120 adhesive. X120 adhesive was chosen mainly due to its easy usage and good strain transfer property (HBM, 2019b). Another consideration was that the stiffness of the adhesiveness is smaller than that of the pile so that the local gauge hardening effect can be avoided. Placing two optical fibres in an extension-compression configuration, i.e., diametrically opposed as shown in Figure 2a, aimed to compensate the temperature effect on the measurement. This effect can be compensated by averaging the difference of the two measured strains (i.e., $\varepsilon_{av.} = (\varepsilon_{ext.} - \varepsilon_{comp.})/2$) as a temperature change has identical effect on both fibres in terms of the peak wavelength shift, e.g., one fibre being compressed and features a negative strain, whereas the other being stretched and has a positive strain. Within each optical fibre, 13 FBGS were integrated and distributed every 25 mm for the first eight FBGS (#1 - #8) and every 50 mm for the rest (#9 - #13). Such a configuration allows to measure the pile strains at 13 different positions ranging from 0 - 425 mm away from the FBGS #1, as shown in Figures 2 and 3.

The calibration of the model pile is intended to compare the the strain measured by FBGS and that calculated from the Euler-Bernoulli beam theory. Two calibrating methods are proposed: i) the pile clamped at one end (i.e., cantilever beam) and ii) the pile put on two rigid supports (e.g., simply supported beam). The apparatus and the corresponding schematic drawing are presented in Figure 3. To avoid the possible damage on the pile end in particular for the cantilever beam configuration where the pile was clamped only 10 mm at the end, the maximum applied weight F was limited, for example 100 N and 500 N for the cantilever and simply supported beam, respectively. For this reason, the calibration strains were within 350 microstrain (10^{-6}), which cannot cover the full range of the following centrifuge tests. Transversal loads were applied at $1\times g$ level with an incremental ratio of about 2, i.e., 20, 50, 100 N for the cantilever beam and 20, 50, 100, 200 and 500 N for the simply supported beam. In order to evaluate the performance of the FBGS under both tensile and compressive conditions, the pile was calibrated at 0° (initial position) and 180° (turning the pile over). As the transversal load increases, the model pile deflects and generates tensile or compressive strains. These strains can be on the one hand calculated based on the direct measurements of the FBGS as shown in Equation 1, and on the other hand determined by the Euler-Bernoulli beam theory using the following formula:

$$\varepsilon = \frac{MD}{2EI} \tag{2}$$

where M is the moment at different sections, F, the applied transversal force, D, the outside diameter of the pile, E, the Young modulus of the pile and I, the moment of inertia of the section..

For the cantilever beam configuration, the moment M is:

$$M \; = F \cdot (500 + z_{FBGS}) \tag{3}$$

and for the simply supported beam, the moment M is:

$$M \; = \frac{F \cdot 215 \cdot (440 - z_{FBGS})}{955} \tag{4}$$

where z_{FBGS} is the position of the FGBS in mm, as illustrated in Figure 3.

Figure 4 presents the calibration results of the model pile. When the pile is clamped on one tip (i.e., cantilever beam), the transversal loads applied on the other tip generate bending moment, shear force and normal stress at the cross-section of the pile. On the upper side of the neutral axis, the normal stresses and strains are tensile, and on the lower side, they are compressive. The strains measured by the two optical fibres (A and B) are presented in the first and second diagrams of Figure 4a, which correspond to the pile at the initial position and turned 180° over, respectively. For the applied loads, most experimental results (i.e., points) situate on or are very close to the correlation lines according to the Euler-Bernoulli beam theory, i.e., Equation 2. Exceptions are the measurements by the FBGS #13, as shown in Figure 4a. The strains measured by FBGS #13 deviate the theoretical values and the difference becomes more pronounced at larger load levels (e.g., 100 N). The main reason for such inaccurate measurements is that the FBGS #13 is too close (i.e., 15 mm) to the clamp, where shear strains are more significant. In such case, both the Saint Venant principle and the Euler-Bernoulli beam assumptions are not satisfied. The relative difference of the strain measured by FBGS (ε_{FBGS}) and that determined by Euler-Bernoulli beam theory ($\varepsilon_{E\text{-}B}$) ranges from -4.74 to 3.46% for optical fibre A at initial and 180° turn-over positions if the FBGS #13 is not taken into account. Taking the average value of the four measured strains (i.e., fibre A at 0° and 180°, and fibre B at 0° and 180°), the bending moments are calculated with Equation 2 and then compared with the theoretical correlation lines, as shown in the third diagram in Figure 4a. Apart from the last point by FBGS #13, the experimental points are in very good agreement with the theoretical prediction.

When the pile is supported by two tips (i.e., simply supported beam) and the transversal loads are applied in between, strains are in tension on the lower side and in compression on the upper side. Similarly, the experimental points, excluding those measured by FBGS #13, are located around the correlation lines (Figure 4b). However, for the maximum transversal load, the measured strains are deviated from those calculated according to Euler-Bernoulli beam theory. The FBGS measurements derivate from -11.99 to 4.89% from the theoretical predictions for FBGS #1-8. The relative difference increases significantly for FBGS #9-13. This may result from many aspects in such a free system where both the stress concentration and pile movement are possible. As concerning the moment profiles, results in the third diagram of Figure 4b shows better accordance between the experiment and theoretic correlations, with their difference generally smaller than 5%.

4. Pile behaviour under transversal loads in centrifuge test

4.1 Preparation of the centrifuge test

The experimental study was carried out at the IFSTTAR large beam centrifuge (D = 11 m) inaugurated in 1985 (Corté and Garnier, 1986).The centrifuge can generate a maximum gravitational acceleration of 100 g in the bracket for a sample mass up to 2 tons. The FS22DI Industrial

BraggMETERInterrogator box from HBM was placed in the data acquisition chamber that is attached to the rotation centre. The longitude direction of the interrogator was in line with the centrifuge arm. The gravitational acceleration experienced by the interrogator is estimated about 1/15 of the centrifuge basket. The wavelengths of the 13 FBGS at reference scan range from 1520-1580 nm and increase every 5 mm. To prepare for the centrifuge test, three steps were employed: i) model sand preparation, ii) pile installation and iii) load application.

The model soil was the Fontainebleau NE34 poorly graded sand (Table 2). Using the automated raining technique (Garnier 2001), the sand was dropped from a constant height (70 cm in this study) and then pluviated into a 1200 mm (length) by 800 mm (width) by 720 mm (height) rectangular strongbox. The depth of the sand mass was 560 mm and the relative density was 81%. To simulate the prototype condition where the foundation is under water, the sand was saturated by slowly (about 6 hours) injecting water through four draining channels located at the bottom of the strongbox. The attained water table was about 30 mm above the sand surface. The effective volumetric weight of the saturated sand was 10.3 kN/m^3.

Concerning the pile installation, the instrumented model pile (Figure 2) was pushed into the sand at 1×g level by a hydraulic jack. The jacking speed was 1 mm/s and the attained depth is 450 mm, i.e., 9D. The sand level inside the pile was checked and there was no plug generated. After pile installation, an electric actuator was mounted on two supporting beams that perpendicularly placed on the longitudinal edges of the strongbox. The actuator has a stroke of 150 mm and can measure the load with a precision of 0.1 N for a range from 0 - 5 kN. At the end of the piston, a force transducer and a loading fork were integrated, aiming to measure and control the applied horizontal load. In front of the actuator, a laser displacement transducer, with measuring range of 120 mm and resolution of 20 μm, was fixed on a supporting beam. This allows to monitor the pile deflection at 410 mm above the ground level. The established experimental set-up is schematically shown in Figure 5.

Centrifuge test was performed at 100×g level. Horizontal load was applied through the centre of the cross section by pushing the steel rod that crosses the monopile perpendicularly to the instrumentation plan (Figures 2 and 3). The loading point situates at 500 mm (i.e. 10D) above the ground level. The loading was displacement-controlled with a rate of 1 mm/s at the actuator level and terminates at 50 mm (i.e. 1D). The measurements of the FBGS, the laser and force transducer were recorded and registered every 0.02 second (i.e., 50 Hz).

4.2 Horizontal response of the model pile

In Figure 6a, the normal strains measured at each incremental force (every 0.25 kN until 1.75 kN) were plotted versus the pile depth As the applied horizontal load H increases, the normal strains within the pile increase as well. Under the same H, normal strains first slightly increase with depth, reach to the maximum at the depth of 100 mm and then decrease almost to zero at 425 mm below the ground level. The average value of the tensile and compressive strains was used to determine the bending moments and the used equation was shown in Figure 6b. At the ground level, the moments measured by FBGS (empty circular points) are very close to the moments calculated from H (solid square points), confirming the reliability of the FBGS under flight condition. At the pile end (FBGS #13, z = 425), the bending moments are close to zero. The discrete moments along the depth need to be fitted into continuous so that further calculation can be proceeded. In Haiderali and Madabhushi (2016), the authors compared different curve fitting techniques and found that the cubic and cubic B-splines gave more consistent and accurate P-y curves. In this study, the cubic splines function was used to interpolate the experimental results. According to the beam theory, the shear force V and the transversal distributed loads along the pile P (equal to the soil reaction) can be obtained by solving the first and second derivatives of the moment profiles (i.e. cubic splines), respectively. Due to the lack of the experimental results above the ground surface and below the pile tip, the algorithm of the cubic spline forces the spline approximate the end points (i.e., FBGS #1 and FBGS #13) in a default way, considering the second derivative of the spline to be zero. Such algorithm is normally reasonable for FBGS #1 as the second derivative of the bending moment (i.e., soil reaction) should be theoretically null at the ground level, however, probably incorrect for FBGS #13 because the soil reaction at the pile tip should not be zero. As a result, the first and second derivatives of FBGS #13 (i.e. pile depth from 375-425) are not necessarily significant and were not determined. In Figures 6c and 6d, the *V* and *P* profiles are presented. For the former, *V* at the ground level are coherent with *H* applied by the actuator. Slight difference is due to uncertainties in finding the first derivative accurately as it lacks experimental points above the ground surface. Concerning the *P* profile, as *H* increases, the pile rotation centre defined here as the point where the soil reaction is nil, $P = 0$ increases from 210 – 275 mm (i.e., 4.2 – 5.5 D) below the ground level.

Finding the second-order definite integral of the moment profiles, one may obtain the pile transversal deflection *y*. This was usually achieved by solving a simultaneous equation that contains two integration constants. Two limit conditions are introduced in this study. The first one is the pile deflection measured by the electric actuator at the pile head. The second is the null pile deflection ($y = 0$) at the rotation centre, which was determined by finding the depths of the null reaction (P = 0), as presented in El Haffar et al. (2019). Figure 7 presents the pile horizontal deflection at different *H* values. Due to the large embedment depth (i.e., 450 mm or 9*D*), pile deflections are close to zero below the rotation centre (e.g., 300 - 450 mm below the ground surface). Presented also are the pile deflections measured by the laser transducer. As *H* increases, the laser provides extra measurements that are comparable with the measurements provided by the electric actuator.

P-y curves are obtained by plotting the pile deflection *y* versus the soil reaction *P* at different depths (e.g., the depth of the FBGS). In Figure 8, each curve demonstrates the *P-y* relationship as *H* increases from 0.25 – 1.75 kN. *P* is positive above the pile rotation centre and negative under. The initial soil stiffness, i.e., the initial slope of the *P-y* curve, increases as the embedment depth increases (from the ground surface to the pile tip). For the soil at a certain depth (e.g., z = 75 mm), its stiffness decreases as the horizontal load *H* increases. In this study, a plateau is reached only for the second level, z = 25 mm. For deeper levels (e.g. z = 50 – 225 mm), the *P-y* curves show a tendency to be stabilized. However, much more lateral displacement is needed to reach such limit.

5. Conclusions

A model pile was instrumented with two diametrically-opposed optical fibres. The instrumented pile was calibrated at 1×g and then subjected to lateral loading in centrifuge at 100×g. The experimental results show that:

- All the 26 FBGS survived in the 100×*g* centrifuge test;
- At the ground level, the moments determined by FBGS are in accordance with the moments calculated from the transversal force;
- Shear forces at the ground level are slightly larger than the applied transversal forces. Such difference mainly results from the difficulty of the accurate derivation operation at the ground level.
- The pile local behaviour is characterized: under the effect of the increasing horizontal load, pile rotates at the depth 210 - 275 mm (i.e., 4.2 - 5.5*D*) below the ground level. Due to the large embedment depth, the pile deflection below the rotation centre close to zero. The P-y curves at different depths were also determined.

Table 1. Geometric and mechanical characteristics of the pile

Material	Prototype	Model
L (m)	50	0.5
D (m)	5	0.05
d (m)	4.5	0.045
E (GPa)	74 GPa	74 GPa
EI ($N.m^2$)	7.8×10^{11}	7.8×10^{3}

Table 2. Characteristics of the Fontainebleau NE34 sand

Sand	C_u $(=d_{60}/d_{10})$	d_{50} (µm)	$\rho_{d\text{-}min}$ (g/cm^3)	$\rho_{d\text{-}max}$ (g/cm^3)
NE34	1.53	210	1.434	1.746

Acknowledgement

This work benefited from France Energies Marines and State finance managed by the National Research Agency under the Investments for the Future program bearing the reference SOLCYP+ ANR-10-IEED-0006-18. Assistances from the technical staffs of the centrifuge group and discussion with Dr. Thierry Dubreucq are acknowledged.

Reference

Abadie, C. N., Byrne, B. W., & Houlsby, G. T. (2018). Rigid pile response to cyclic lateral loading: laboratory tests. Géotechnique, https://doi.org/10.1680/jgeot.16.P.325.

Barbosa, P., Geduhn, M., Jardine, R. J., & Schroeder, F. C. (2017). Large Scale Offshore Static Pile Tests-Practicality and Benefits. In Proceeding of 8th International Conference of Offshore Site Investigation Geotechnics, London, (2): 644-651.

Baguelin, F. et Jézéquel, J. (1972). Etude expérimentale du comportement de pieux sollicités horizontalement. *Bulletin de Liaison des Ponts et Chaussées*, 62, 129-170.

Byrne, B. W., McAdam, R. A., Burd, H. J., Houlsby, G. G., Martin, C. M., Beuckelaers, W. J. A. P., … & Ushev, E. (2017). PISA: New Design Methods for Offshore Wind Turbine Monopiles. In Proceeding of 8th International Conference of Offshore Site Investigation Geotechnics, London, (1): 142-161.

Choo, Y. W., & Kim, D. (2015). Experimental Development of the p-y Relationship for Large-Diameter Offshore Monopiles in Sands: Centrifuge Tests. Journal of Geotechnical and Geoenvironmental Engineering, 142(1), 04015058.

Correia, R., James, S. W., Marshall, A., Heron, C., & Korposh, S. (2016). Interrogation of fibre Bragg gratings through a fibre optic rotary joint on a geotechnical centrifuge. In Sixth European Workshop on Optical Fibre Sensors (Vol. 9916, p. 99162B). International Society for Optics and Photonics.

Corté, J. F., & Garnier, J. (1986). Une centrifugeuse pour la recherche en géotechnique. Bulletin de Liaison des Laboratoires des Ponts et Chaussées, 146, 5-28.

Cox, W. R., Reese, L. C., & Grubbs, B. R. (1974). Field testing of laterally loaded piles in sand. In Offshore Technology Conference (OTC 2079): 459 - 472.

Da Silva, T. S., Elshafie, M. Z. E., & Sun, T. (2016). Fibre optic instrumentation and calibration in the geotechnical centrifuge. Proceeding of the 3rd European Conference on Physical Modelling in Geotechnics, Nantes, France, 129-135.

Davisson, M., & Salley, J. (1969). Lateral load tests on drilled piers. Performance of Deep Foundations, ASTM STP 444, 68-83.

Doherty, P., Igoe, D., Murphy, G., Gavin, K., Preston, J., McAvoy, C., Byrne, B. W., Mcadam, R., Burd, H. J., Houlsby, G. T., Martin, C. M. (2015). Field validation of fibre Bragg grating sensors for measuring strain on driven steel piles. Géotechnique Letters, 5(2), 74-79.

El Haffar, I., Blanc, M., & Thorel, L. 2019. Monotonic lateral loading on single piles in sand: parametric centrifuge modelling in eccentricity, saturation and installation mode. Géotechnique (submitted).

France Energies Marines. (2017). SOLlications CYcliques des monoPieux d'éoliennes offshore. Accessed on: 2019-04-11. **URL**: https://solcyp.france-energies-marines.org/

Garnier, J. (2001). Modèles physiques en géotechnique-I–Évolution des techniques expérimentales et des domaines d'application. Revue Française de Géotechnique, (97), 3-29.

Garnier, J. (2013). Advances in lateral cyclic pile design: contribution of the SOLCYP project. In Proceedings of the TC 209 Workshop: 18th ICSMGE–Design for Cyclic Loading: Piles and Other Foundations, Paris, France, 59-68.

Georgiadis, M., Anagnostopoulos, C., & Saflekou, S. (1992). Centrifugal testing of laterally loaded piles in sand. Canadian Geotechnical Journal, 29(2), 208-216.

Glisic, B., & Yao, Y. (2012). Fiber optic method for health assessment of pipelines subjected to earthquake-induced ground movement. Structural Health Monitoring, 11(6), 696-711.

Haiderali, A. E., & Madabhushi, G. (2016). Evaluation of curve fitting techniques in deriving p–y curves for laterally loaded piles. Geotechnical and Geological Engineering, 34(5), 1453-1473.

HBM (2019a). Optical Measurement Solutions. Accessed on: 2019-04-09. **URL:** https://www.hbm.com/fileadmin/mediapool/local/.../HBM-FiberSensing_US_web.pdf

HBM (2019b). X120 adhesive special features. Accessed on: 2019-06-16. **URL:** https://www.hbm.com/fileadmin/mediapool/hbmdoc/technical/B05001.pdf

Hill, K. O., & Meltz, G. (1997). Fiber Bragg grating technology fundamentals and overview. Journal of Lightwave Technology, 15(8), 1263-1276.

Hong, C. Y., Zhang, Y. F., Zhang, Y. W., Borana, L., & Wang, R. F. (2017). New LGFBG-Based structural integrity evaluation method for cement-Grouted soil nails. International Journal of Geomechanics, 17(8), 04017026.

Hussaini, S. K., Indraratna, B., & Vinod, J. S. (2015). Application of optical-fiber Bragg grating sensors in monitoring the rail track deformations. Geotechnical Testing Journal, 38(4), 387-396.

Jardine, R.J., Buckley, R.M., Kontoe, S., Barbosa, P. & Schroeder, F.C. (2018). Behaviour of piles driven in chalk. Engineering in Chalk. 33-51

Kapogianni, E., Sakellariou, M. G., Laue, J., & Springman, S. M. (2010). The use of optical fibre sensors in a geotechnical centrifuge for reinforced slopes. Proceedings of the 7th International Conference on Physical Modelling in Geotechnics, Zurich, Switzerland. Vol. 1, 343-348.

Klinkvort, R. T., & Hededal, O. (2013). Lateral response of monopile supporting an offshore wind turbine. Proceedings of the ICE-Geotechnical Engineering, 166(2), 147-158.

Klinkvort, R. T., & Hededal, O. (2014). Effect of load eccentricity and stress level on monopile support for offshore wind turbines. Canadian Geotechnical Journal, 51(9), 966-974.

Klinkvort, R. T., Britta Bienen B., Fan, S., Black, J., Bayton, S., Thorel, L., Blanc, M., Madabhushi, G., Haigh, S., Broad, T., Zania, V., Askarinejad, A., Li, Q., Kim, D. S., Park, S. (2019). Centrifuge modelling considerations of laterally loaded monopiles in sand. Géotechnique (submitted).

Klinkvort, R. T., Hededal, O., & Springman, S. M. (2013). Scaling issues in centrifuge modelling of monopiles. International Journal of Physical Modelling in Geotechnics, 13(2), 38-49.

Koukoura, C., Natarajan, A., & Vesth, A. (2015). Identification of support structure damping of a full scale offshore wind turbine in normal operation. Renewable Energy, 81, 882-895.

Kreuzer, M. (2006). Strain measurement with fiber Bragg grating sensors. HBM, Darmstadt, S2338-1.0 e.

LeBlanc, C., Houlsby, G. T., & Byrne, B. W. (2010). Response of stiff piles in sand to long-term cyclic lateral loading. Géotechnique, 60(2), 79-90.

Lee, W., Lee, W. J., Lee, S. B., & Salgado, R. (2004). Measurement of pile load transfer using the Fiber Bragg Grating sensor system. Canadian Geotechnical Journal, 41(6), 1222-1232.

Li, Z., Haigh, S. K., & Bolton, M. D. (2010). Centrifuge modelling of mono-pile under cyclic lateral loads. Proceedings of the 7th International Conference on Physical Modelling in Geotechnics, Zurich, Switzerland, 965–970

Little, R. L., & Briaud, J. L. (1988). Full scale cyclic lateral load tests on six single piles in sand. Miscellaneous Paper GL-88-27, Geotechnical Division, Texas A&M University, College Station, Texas 77843

McAdam, R., Byrne, B.W., Houlsby, G., Beuckelaers, W.J.A.P., Burd, H., Gavin, K., Igoe, D., Jardine, R., Martin, C., Muir Wood, A. & Potts, D. (2018). Monotonic lateral loaded pile testing in a dense marine sand at Dunkirk. Géotechnique.

Ng, C.W.W., Shi, C., Gunawan, A., Laloui, L., and Liu, H.L. 2015. Centrifuge modelling of heating effects on energy pile performance in saturated sand. Canadian Geotechnical Journal 52(8): 1045-1057.

Ni, P., Moore, I.D., and Take, W.A. 2018. Distributed fibre optic sensing of strains on buried full-scale PVC pipelines crossing a normal fault. Géotechnique 68(1): 1-17.

Park, S., Park, T., & Han, K. (2011). Real-time monitoring of composite wind turbine blades using fiber Bragg grating sensors. Advanced Composite Materials, 20(1), 39-51.

Puech, A. and Garnier, J. (2017). Design of piles under cyclic loading: SOLCYP recommendations. Wiley-ISTE, 454 pages.

Reese, L. C., Cox, W. R., & Koop, F. D. (1974). Analysis of laterally loaded piles in sand. In Offshore Technology Conference (OTC 2080), 473 - 483.

Rosquoet, F., Thorel, L., Garnier, J., & Canepa, Y. (2007). Lateral cyclic loading of sand-installed piles. Soils and Foundations, 47(5), 821-832.

Simpson, B., Hoult, N. A., & Moore, I. D. (2015). Distributed sensing of circumferential strain using fiber optics during full-scale buried pipe experiments. Journal of Pipeline Systems Engineering and Practice, 6(4), 04015002.

Saiyar, M., Ni, P., Take, W.A., and Moore, I.D. 2016. Response of pipelines of differing flexural stiffness to normal faulting. Géotechnique 66(4): 275-286.

Ting, J. M. (1987). Full-scale cyclic dynamic lateral pile responses. Journal of Geotechnical Engineering, 113(1), 30-45.

Truong, P., Lehane, B. M., Zania, V., & Klinkvort, R. T. (2018). Empirical approach based on centrifuge testing for cyclic deformations of laterally loaded piles in sand. Géotechnique, 69(2), 133-145.

Verdure, L., Garnier, J., & Levacher, D. (2003). Lateral cyclic loading of single piles in sand. International Journal of Physical Modelling in Geotechnics, 3(3), 17-28.

Weng, X., Zhao, Y., Lou, Y., & Zhan, J. (2016). Application of Fiber Bragg Grating Strain Sensors to a Centrifuge Model of a Jacked Pile in Collapsible Loess. Geotechnical Testing Journal, 39(3), 362-370.

Wind Europe. (2017). 'The European onshore wind industry - key trends and statistics 2016'. Accessed on: 2016-07-03.

Zhu, H. H., Yin, J. H., Jin, W., & Zhou, W. H. (2007). Soil nail monitoring using Fiber Bragg Grating sensors during pullout tests. The Joint 60th Canadian Geotechnical and 8th IAH-CNC Conferences. Ottawa, Canada, 821-828.

Zhu, H. H., Yin, J. H., Yeung, A. T., & Jin, W. (2011). Field pullout testing and performance evaluation of GFRP soil nails. Journal of Geotechnical and Geoenvironmental Engineering, 137(7), 633-64.

FIGURE CAPTIONS

Figure 1 Working principle of the Fibre Bragg Grating sensors

Figure 2 Instrumentation of the model pile

Figure 3 Experimental set-up for the calibration of the instrumented pile

Figure 4 Measurements of the FBG sensors for the calibration test

Figure 5 Schematic drawing of the transversal loading system in the centrifuge

Figure 6 Profile of (a) the measured strains, (b) the bending moment, (c) the shear force and (d) the soil reaction (i.e., the distributed load)

Figure 7 Deflection of the pile below and above the ground level

Figure 8 Soil reaction (P) versus the normalized pile deflection (y/D)

FIGURE CAPTIONS

Figure 1 Working principle of the Fibre Bragg Grating sensors

Figure 2 Instrumentation of the model pile

Figure 3 Experimental set-up for the calibration of the instrumented pile

Figure 4 Measurements of the FBG sensors for the calibration test

Figure 5 Schematic drawing of the transversal loading system in the centrifuge

Figure 6 Profile of (a) the measured strains, (b) the bending moment, (c) the shear force and (d) the soil reaction (i.e., the distributed load)

Figure 7 Deflection of the pile below and above the ground level

Figure 8 Soil reaction (P) versus the normalized pile deflection (y/D)

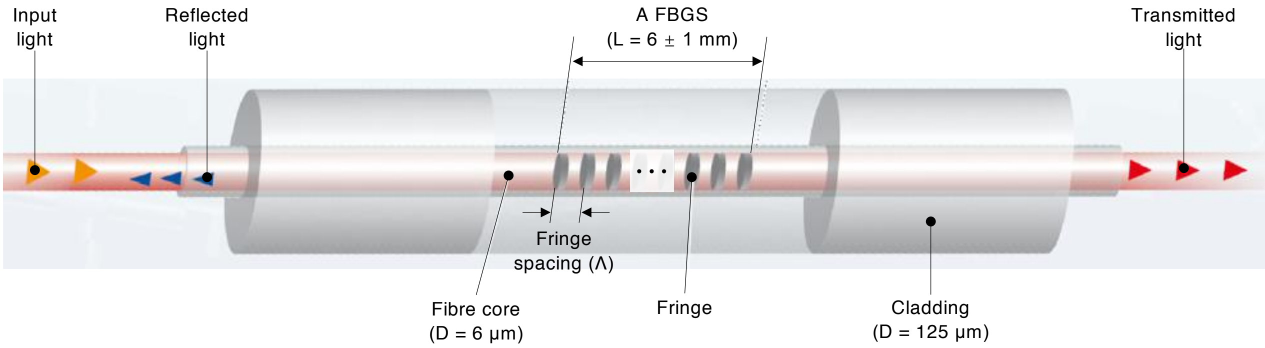

(a) Composition of the fibre (after HBM, 2019a)

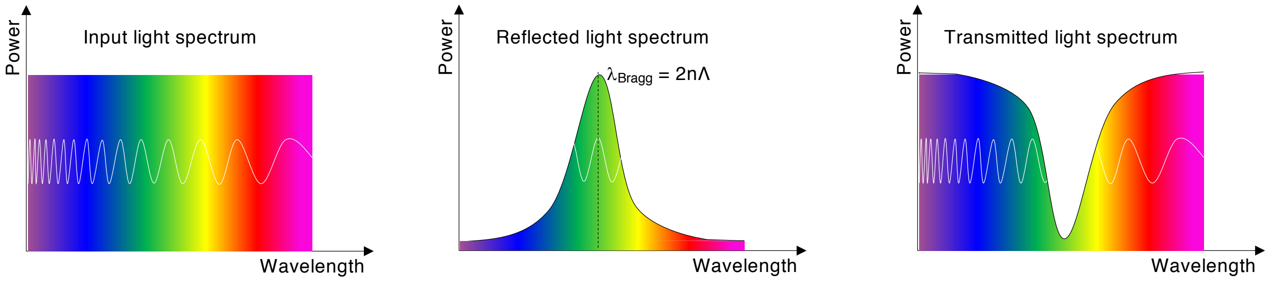

(b) Wave propagation in the Bragg optical fibre

Figure 1 Working principle of the Fibre Bragg Grating sensors

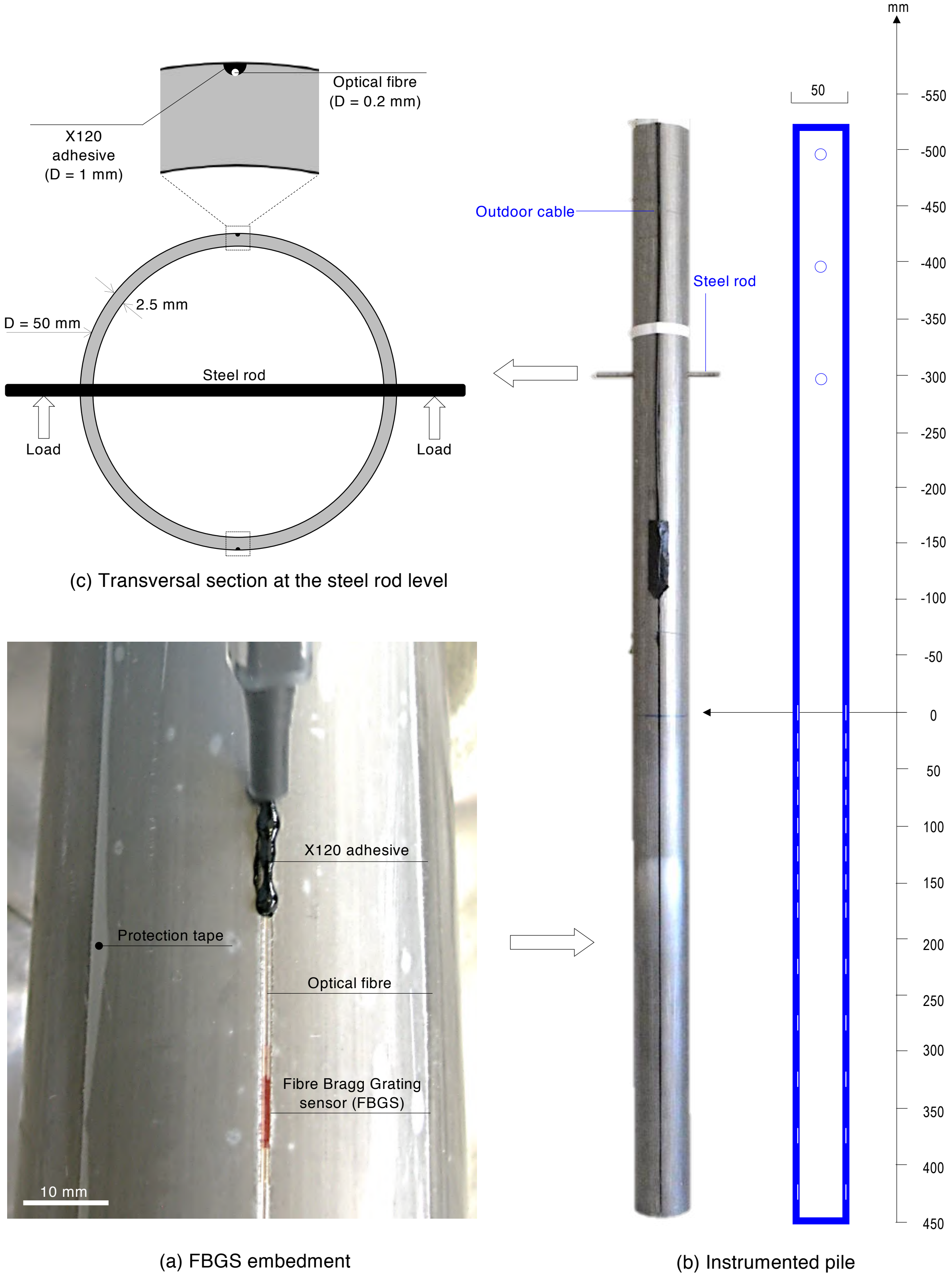

Figure 2 Instrumentation of the model pile

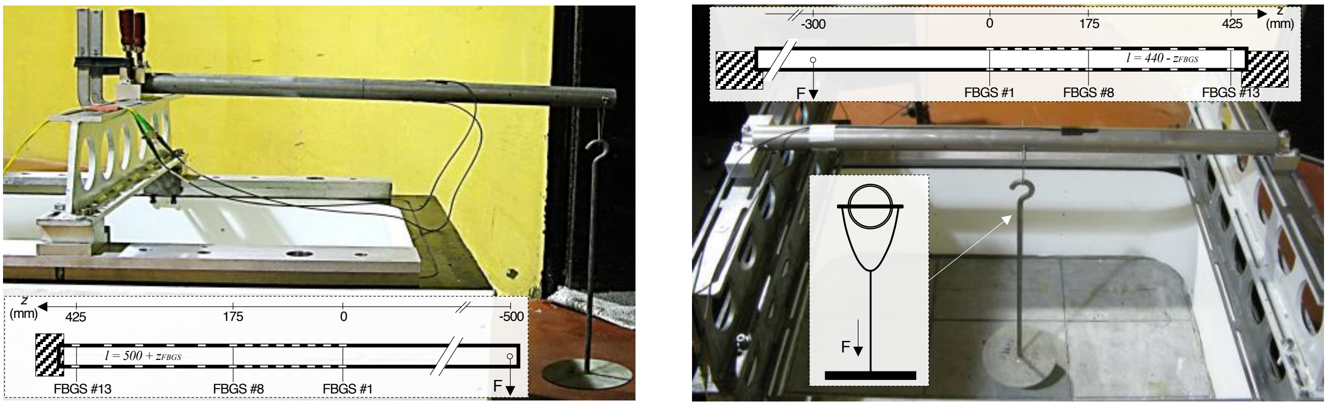

(a) Cantilever beam configuration

(b) Simply supported beam configuration

Figure 3 Experimental set-up for the calibration of the instrumented pile

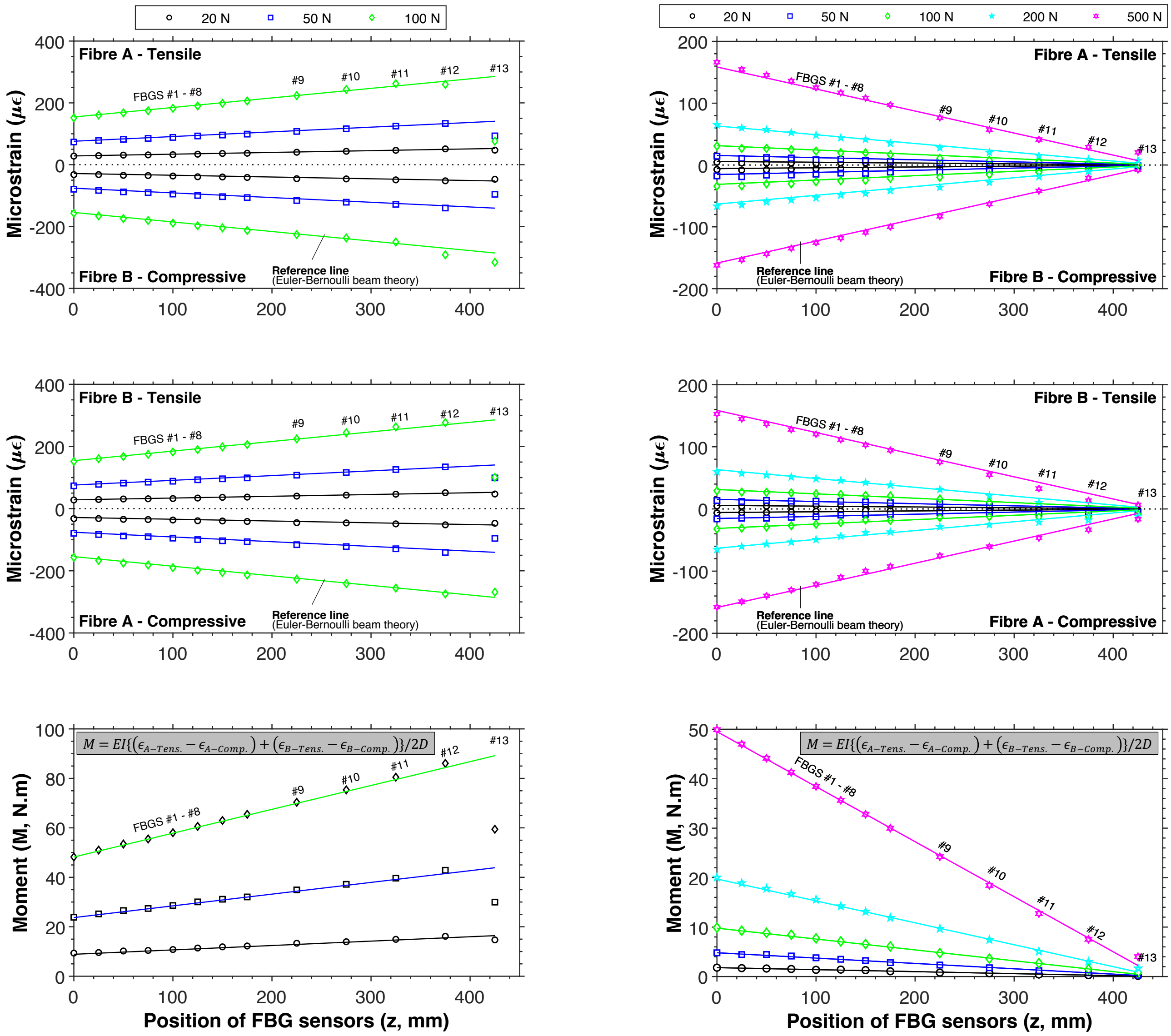

(a) Cantilever beam

(b) Simply supported beam

Figure 4 Measurements of the FBG sensors for the calibration test

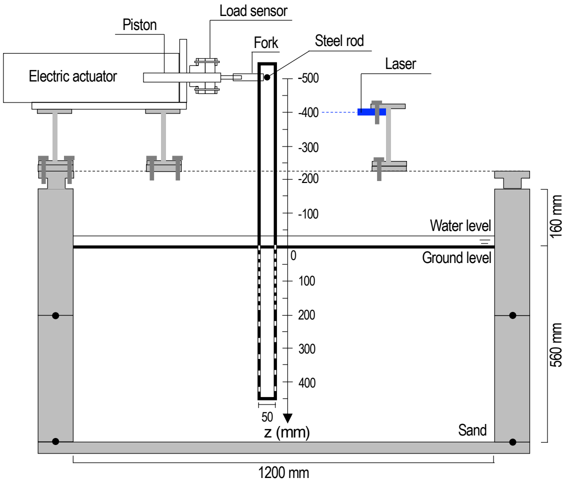

Figure 5 Schematic drawing of the transversal loading system in the centrifuge

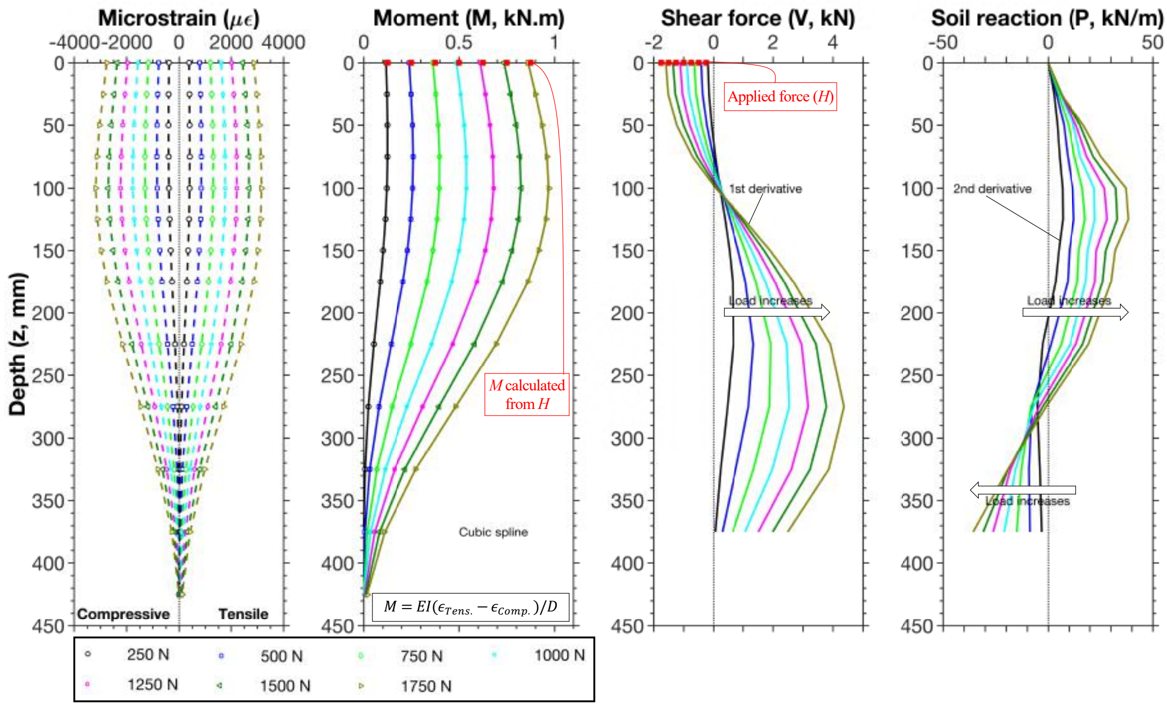

Figure 6 Profile of (a) the measured strains, (b) the bending moment, (c) the shear force and (d) the soil reaction (i.e., the distributed load)

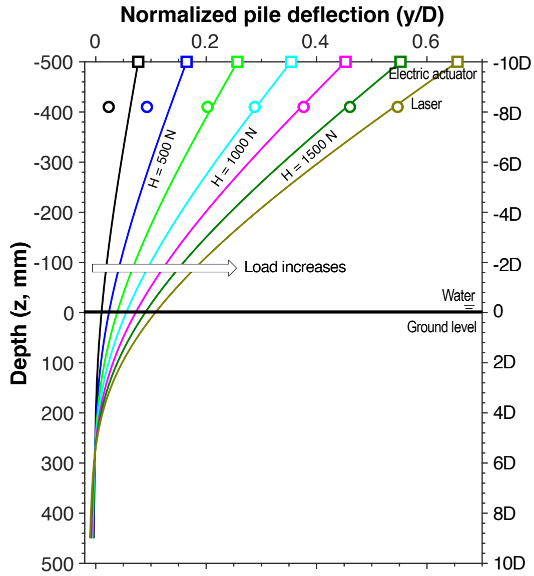

Figure 7 Deflection of the pile below and above the ground level

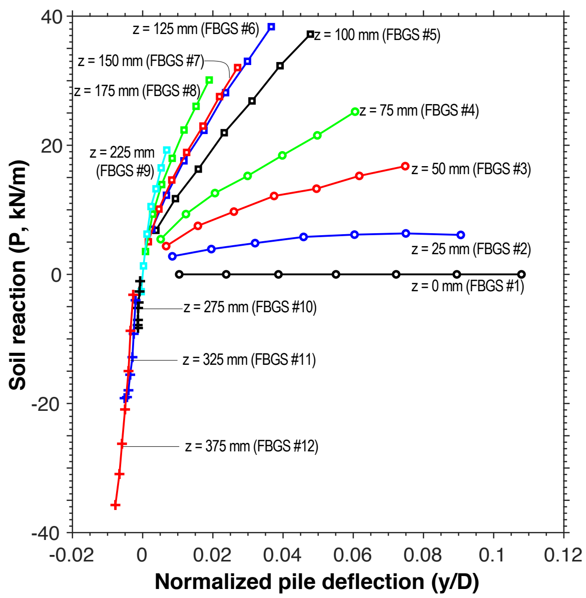

Figure 8 Soil reaction (P) versus the normalized pile deflection (y/D)